Supplementary materials

Section 1 is the grid independence study of the laminar flow calculation, as stated in Section 3.1 in the article. Section 2 provides the solver verification for the cases of crossflow instability, as described in Section 3.2 in the article. Section 3 gives the details of the preparatory analysis of SIT in Section 7.1 in the article.

1. Grid independence study

To cluster more points within the boundary layer, two clustering distribution functions are adopted in the wall-normal direction for the laminar flow calculation. First clustering:

$$\zeta' = \frac{1 - \tanh c_0}{1 - \tanh\left(c_0 \frac{\zeta - 1}{N_y - 1}\right)} (\zeta - 1) + 1, \qquad \zeta = 1, 2, \cdots, N_y \qquad (1.1a)$$

where N_y is the number of grid points, $\zeta' \in [1, N_y]$ and $c_0 \geqslant 0$ is the controlling parameter. The larger c_0 is, the more grids are in the boundary layer. Second clustering:

$$\eta = \eta_{\max} \frac{\zeta' - 1}{b_0 - 2a_0\zeta'}, \quad a_0 = \frac{1 - 2\vartheta}{2\vartheta}, \quad b_0 = (1 + 2a_0)(N_y - 1) + 2a_0 \qquad (1.1b)$$

where the second controlling parameter $\vartheta \in (0, 1)$ is the relative location of the midpoint, and $\eta_{\max}$ is the distance between the wall and the shock. To determine the required N_y, three calculations are performed with N_y of 201, 401 and 801, respectively. Figure 1 compares the results of both the laminar flow (second-order derivative of temperature) and the instability (growth rate of stationary crossflow mode). As can be seen, the results with $N_y = 401$ are nearly identical to those with $N_y = 801$, while the growth rate curve with $N_y = 201$ has minor deviations from the other two. Therefore, $N_y = 401$ is adopted for the calculations presented in the article.

2. Verification of instability solvers

The present instability solvers for TCNE flows have been verified in the authors' previous works (see Chen *et al.* 2021*a*,*b*). Besides, we calculate some previous cases on crossflow instability for comparison. The first is a Mach-3 swept-cylinder case studied by Balakumar & King (2012). The cylinder radius is 30 mm, $\Lambda = 50°$, and $Re_\infty = 2.83 \times 10^6$ /m. The growth rates of stationary and travelling crossflow modes are calculated using LST. As shown in figure 2, excellent agreement with the reference data is obtained.

The second case is a Mach-6 swept-parabola case studied by Xu *et al.* (2019). Λ is 45° and $Re_\infty = 8 \times 10^6$ /m. The nonlinear evolution of mode (0, 1) with $\lambda_z = 10$ mm is calculated using the NPSE solver under the CPG assumption. Figure 3 gives the disturbance amplitudes of different modes, and the results are agreeable with the reference.

Finally, a Mach-13 swept-wing case by Kline *et al.* (2018) is calculated, which is one of the very few cases concerning both crossflow instability and high-temperature effects. The wing geometry is displayed in figure 4(*a*). Here the chord length is 2 m, the thickness is 0.4 m, and the nose radius is 0.5 mm. The free-stream conditions correspond to an altitude of 30 km, the wall is adiabatic, and the angles of sweep and attack are 60° and −4°, respectively. The flow was assumed to be thermal equilibrium and chemical non-equilibrium (TECN) by Kline *et al.* (2018), so the calculations under the TECN assumption are also performed, by multiplying Q_{t-v} by a factor of 10^4 (Hudson 1996). The comparison of the N factors of stationary crossflow modes is shown in figure 4(*b*), and good agreement is obtained. The small difference is due to the different model parameters of chemical reaction rates
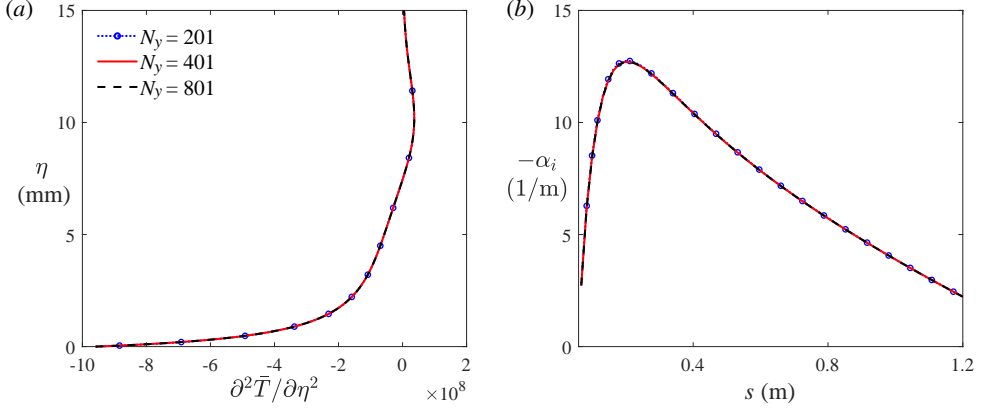
Figure 1: (*a*) Second-order wall-normal derivative of temperature, and (*b*) the growth rate of stationary crossflow mode ($\lambda_z = 40$ mm) by using different N_y
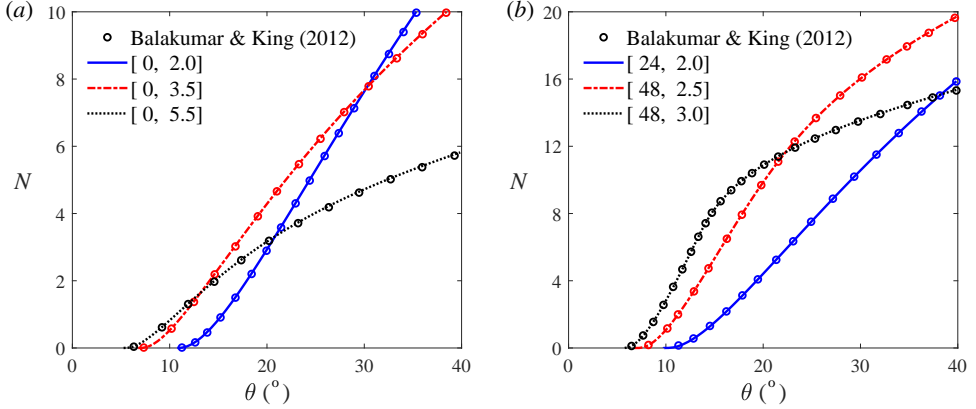

Figure 2: *N* factor curves of (*a*) stationary and (*b*) travelling crossflow modes in the Mach-3 swept-cylinder case. The reference LST data is from Balakumar & King (2012). θ is the circumferential angle measured from the leading edge. The notation in the legend denotes the mode with [f in kHz, λ_z in mm].

and molecular collision integrals. Furthermore, we calculate the growth rates of stationary modes under the CPG, TECN and TNCN (i.e. TCNE) assumptions, respectively, as shown in figure 4(*c*). The non-equilibrium effects are observed to be slightly stabilizing. Further analysis shows that the crossflow Mach number $Ma_{\rm cf}$, as discussed in the article, in the CPG case is also the largest, so the positive correlation between the crossflow Mach number and the mode growth rate also holds for this flow. At last, it is worth mentioning that the CPG results in figure 4(*c*) have deviations from those in Kline *et al.* (2018), which is possibly due to the different transport models used for CPG flows. The CPG results in the present work adopt the same transport models as those in the TNCN case, while Kline *et al.* (2018) did not mention theirs for the CPG case (maybe Sutherland's law or others).
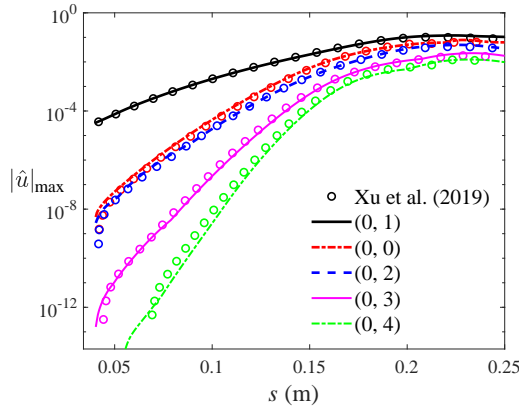
Figure 3: Streamwise distribution of disturbance mode amplitudes in the Mach-6 swept-parabola case. The reference NPSE data is from Xu *et al.* (2019).
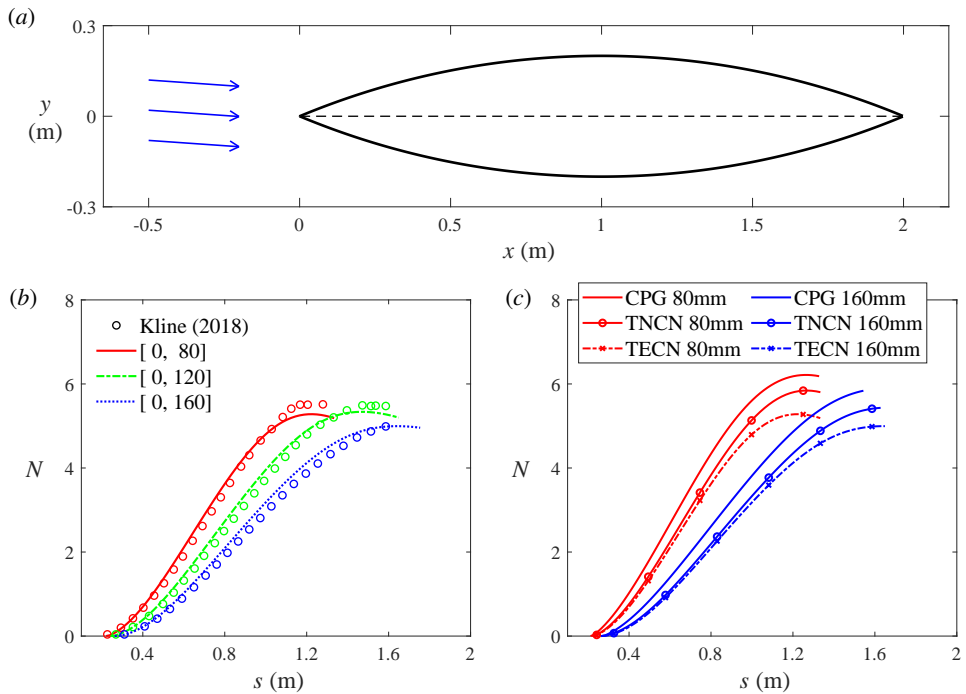

Figure 4: (*a*) is the geometry of the Mach-13 swept-wing case. (*b*) is the N factor curves of stationary crossflow modes in the TECN case with the reference LST data from Kline *et al.* (2018). The notation in the legend denotes the mode with [f in kHz, λ_z in mm]. (*c*) is the N factor curves of stationary crossflow modes in the CPG, TECN and TNCN cases.

3. Preparatory analysis of SIT

A convergence study is conducted here to determine the required N_{sd} for secondary instability calculations. Also, an examination is performed on whether $N_{max} = 32$ in Section 6.1 in the article is adequate to provide an accurate base flow for SIT. First, the base flow with $N_{max} = 32$ is adopted. The eigenvalues ω_s of the three most unstable modes (temporarily termed as M1,

Mode	$N_{sd} = 16$	$N_{sd} = 18$	$N_{sd} = 20$
M1 ($\alpha_s = 126.1$ /m)	$9.565 - 85.323i$	$9.563 - 85.326i$	$9.563 - 85.326i$
M2 ($\alpha_s = 252.1$ /m)	$8.696 - 199.19i$	$8.695 - 199.19i$	$8.695 - 199.19i$
M3 ($\alpha_s = 390.8$ /m)	$8.162 - 309.57i$	$8.158 - 309.57i$	$8.159 - 309.57i$

Table 1: Eigenvalues $\omega_s/Q_\infty[1/m]$ of the three most unstable modes from SIT ($\sigma_d = 0$) with different N_{sd} at $s = 1.0$ m in the TCNE benchmark case.

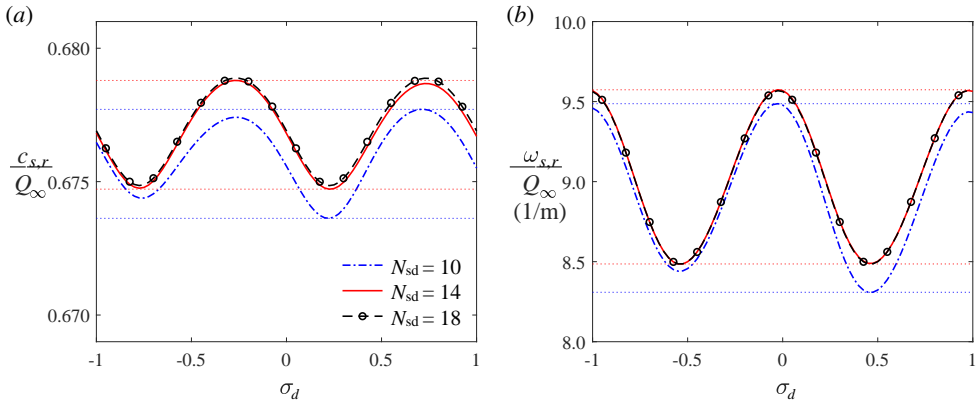

Figure 5: Variations of mode M1's (a) phase velocity $c_{s,r}/Q_\infty$ and (b) growth rate $\omega_{s,r}/Q_\infty[1/m]$ with the Floquet detuning parameter in the TCNE benchmark case. Different N_{sd} are used and $s = 1.0$ m.

M2 and M3 modes) are listed in table 1 with different N_{sd} in the TCNE benchmark case. As can be seen, the relative errors between the results with $N_{sd} = 18$ and 20 are all less than 10^{-4}, so $N_{sd} = 18$ is adopted for the calculation in the article, which is comparable with those required for lower-speed flows (Koch *et al.* 2000; Xu *et al.* 2019). Note that the required N_{sd} here is much larger than that for the second mode where N_{sd} is generally less than 4 (Herbert 1988), so the computational cost is dramatically higher. For a further test of convergence, the variation of mode M1's ω_s with σ_d is also calculated. Theoretically, a fully converged solution should give identical results when σ_d differs by an integer, because this shift in σ_d only replaces the harmonics of the largest spanwise wavenumber in $\tilde{q}_{2,sd}$. As shown in figure 5, the eigenvalues with $N_{sd} = 10$ and 14 are not yet fully converged, while the results with $N_{sd} = 18$ meet the σ_d-periodic requirement. The phase velocity is less sensitive to σ_d than the growth rate, and the latter experiences a variation of $\pm 6\%$ in figure 5(b). Compared with that of the second mode, the effect of σ_d on the secondary crossflow instability is negligible. Therefore, no distinctions are made between the fundamental, subharmonic and detuned modes, and $\sigma_d = 0$ is adopted in the article. In order to assure a justified base flow, the N_{max} in the NPSE calculation is varied, and the secondary crossflow instability is calculated based on different base flows. Figure 6 provides the growth rates of modes M1 and M2 with $N_{max} = 24$, 32 and 40, respectively. As can be seen, the results with $N_{max} = 24$ have relatively large deviations from the others, especially in the high-wavenumber region. The base flow with $N_{max} = 32$ provides adequate accuracy for the secondary instability calculations of stationary crossflow vortices.
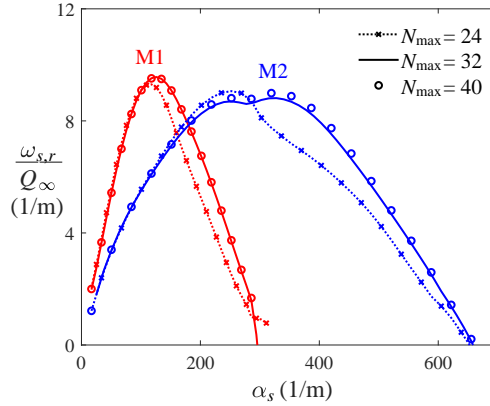
Figure 6: Growth rates of modes M1 and M2 at different streamwise wavenumbers in the TCNE benchmark case. Different $N_{\max}$ are used in the base flow calculations and s is 1.0 m.

REFERENCES

BALAKUMAR, P. & KING, R. A. 2012 Receptivity and stability of supersonic swept flows. *AIAA Journal* **50** (7), 1476–1489.

CHEN, X., WANG, L. & FU, S. 2021*a* Parabolized stability analysis of hypersonic thermal-chemical nonequilibrium boundary-layer flows. *AIAA Journal* **59** (7), 2382–2395.

CHEN, X., WANG, L. & FU, S. 2021*b* Secondary instability of the hypersonic high-enthalpy boundary layers with thermal-chemical nonequilibrium effects. *Physics of Fluids* **33** (3), 034132.

HERBERT, T. 1988 Secondary instability of boundary layers. *Annual Review of Fluid Mechanics* **20**, 487–526.

HUDSON, M. L. 1996 Linear stability of hypersonic flows in thermal and chemical nonequilibrium. PhD thesis, North Carolina State University.

KLINE, H. L., CHANG, C.-L. & LI, F. 2018 Hypersonic chemically reacting boundary-layer stability using LASTRAC. In *2018 Fluid Dynamics Conference*.

KOCH, W., BERTOLOTTI, F. P., STOLTE, A. & HEIN, S. 2000 Nonlinear equilibrium solutions in a three-dimensional boundary layer and their secondary instability. *Journal of Fluid Mechanics* **406**, 131–174.

XU, G., CHEN, J., LIU, G., DONG, S. & FU, S. 2019 The secondary instabilities of stationary cross-flow vortices in a Mach 6 swept wing flow. *Journal of Fluid Mechanics* **873**, 914–941.